

Validation of 3D Adjoint Based Error Estimation and Mesh Adaptation for Sonic Boom Prediction

W. T. Jones* E. J. Nielsen† M. A. Park‡

A procedure used to validate a 3-D mesh adaptation scheme based on adjoint-based error estimation with application to sonic boom propagation is described. The method is based on a cost function formulation that integrates the near-field pressure differential over a prescribed surface. The uncertainty in the computation of this cost function is used to drive automatic h-r mesh adaptation such that errors in the functional are reduced without human intervention. The primary configurations used to validate the technique are a family of simple cone-cylinder geometries for which experimental data is available. Computed results for inviscid flow at Mach numbers of 1.26 and 1.41 are presented at various distances in the near-field up to 20 body lengths. These results are compared against the available test data and show good agreement.

Nomenclature

Δp	incremental pressure due to flow field of model	h	perpendicular distance from model centerline to measurement location
ΔX	distance from point on pressure signature to point where pressure signature curve crosses the zero pressure reference axis	l	model reference length
\mathbf{Q}	flow field dependent variables	M	Mach number
ρ	density	p	free-stream static reference pressure
A	area of cost function surface	r	radius
f	objective function	u, v, w	Cartesian velocity components
g	normalized pressure signature	x	longitudinal distance measured from the model nose
		λ	vector of adjoint variables

I. Introduction

Ongoing interest in supersonic overland flight has continued to drive the need for accurate prediction and subsequent minimization of sonic boom overpressures. Prediction is traditionally provided through the propagation of near-field pressure signatures to the ground. These near-field pressure signatures are typically determined experimentally or computed via Whitham theory^{1,2} for predicting flow characteristics about bodies of revolution. Common propagation techniques involve a quasi-acoustic ray tracing process where the pressure signature is regarded as a locally axisymmetric source.³ Examples of such techniques include the Thomas code⁴ and PCBoom3.⁵ However, this combination of near-field methods with propagation schemes is not reliable if initiated at small distances from the body. This is due to the expectation that the complex acoustic source distributions have coalesced and that there is a lack of cross flow.³ The minimum distance from the body for which this methodology remains valid is therefore dependent on both the source strengths and the existence of cross flow. Such a location is generally regarded as being on the order of tens of body lengths.

In order to accurately predict overpressure for complex geometries typical of aerospace vehicles, a more general method of computing near-field pressures is required to supplement traditional near-field theory. Higher fidelity techniques involving computational fluid dynamics (CFD) methods are an obvious choice as a general alternative for computing near-field pressures. Unfortunately, meshing requirements and computing power have placed a practical

*Senior Member AIAA, Computer Engineer, Advanced Engineering Environments Branch, NASA Langley Research Center (LaRC), Hampton, Virginia.

†Senior Member AIAA, Research Scientist, Computational AeroSciences Branch, NASA LaRC.

‡Member AIAA, Research Scientist, Computational AeroSciences Branch, NASA LaRC.

This material is declared a work of the U.S. Government and is not subject to copyright protection in the United States.

limit on the maximum distance where signatures can be accurately obtained. As a result, pressure data is often extracted at distances of order-1 body length below the vehicle.⁶ At larger distances, mesh size becomes prohibitive and optimal mesh clustering strategies are often insufficient. It is also not uncommon as in Ref. 6 that *a priori* knowledge of the flow field be considered in developing the baseline mesh so as to capture all of the phenomena of interest. This all is in light of traditional feature-based mesh adaptation methodologies. Therefore, prediction of sonic boom signatures using traditional CFD techniques is problematic in that a significant amount of *a priori* knowledge is required in order to generate a mesh with sufficient resolution and character so as to propagate shock waves far into the near-field and due to the expense of ad hoc mesh refinement to said distances.

Until recently, feature-based mesh adaptation provided the primary means to enhance the propagation of shock waves through refinement of the mesh subject to local flow field feature gradients. While this method is often successful in identifying features, it usually results in a mesh that overemphasizes discontinuities, which generally tend to dominate the flow fields that characterize sonic boom studies. A requirement implicit in feature-based adaptation strategies is that the mesh to be refined must possess some semblance of initial flow field gradients. In other words, if the reference flow field lacks gradients due to an overly coarse mesh, the feature based techniques will fail to recognize the need for mesh refinement. Moreover, if the location of flow features computed using the initial mesh is incorrect, the adaptation strategy can converge to the wrong result.⁷ Finally, these techniques give little insight as to the error in the calculation, nor do they ensure that each of the discontinuities, while highly resolved, actually influence the sonic boom on the ground (e.g., shock waves above the vehicle may be resolved unnecessarily).

Recent advances in the field of adaptation include the use of error estimators based on the adjoint solution to the flow equations. These novel methods seek to improve the accuracy of a given engineering output such as lift or drag. This output-based approach has been applied to finite element discretizations and includes applications to error bounds on outputs and adaptation.^{8–15}

The error correction methodology was extended to discretizations other than finite elements by Pierce and Giles.¹⁶ Müller and Giles¹⁷ later applied an adaptive technique to reduce the error correction term for finite volume solutions. Venditti and Darmofal^{18,19} demonstrated an adaptive technique for compressible 2-D inviscid and viscous flow solutions, which improves the error correction of an output function. Their method for anisotropic adaptation of 2-D turbulent flows was demonstrated on a multi-element airfoil. Reference 18 demonstrates significant improvement in the reliability and output accuracy of the adjoint-based method in comparison with pure Hessian-based (feature-based) adaptation. This output-based approach provides a natural termination criteria that is based on a user-specified functional error tolerance. An added benefit of an output-based adaptive process is that it holds the promise of lowering quality requirements on the initial mesh generation process because the output-based adaptation is able to find the correct solution given extremely coarse initial meshes.^{18–21} These initial meshes may be unable to resolve important features that are present in the final adapted mesh. However, after a number of iterations, the adjoint-adapted meshes have implicitly positioned and resolved these features. This lower resolution and quality requirement directly increases the robustness and reduces the work-hours associated with the initial mesh generation process. The initial mesh resolution specification may also be formulated to automatically satisfy these reduced resolution requirements. Output-based adaptation has considerable potential to reduce the expense and increase the robustness and accuracy of CFD solutions for 3-D problems. However, the mesh adaptation mechanics to realize this process improvement for general 3-D high Reynolds number applications are not well established at this time.

Park^{20,21} extended the error-estimation methods in Ref. 18 to 3-D inviscid, laminar, and turbulent flows. Reference 21 demonstrated automated output (adjoint) anisotropic surface and field adaptation on an inviscid ONERA M6 wing and manual adaptation of a turbulent, extruded NACA 0012 airfoil. The error estimation procedure in Ref. 21 required the sequential computation of the flow and adjoint residual on an h-refined embedded mesh. This sequential execution process limited the size of the problems that could be analyzed on distributed computer clusters. A parallel method of execution has been implemented and applied to 3-D, large scale, realistic aerospace applications.²² Robust adaptation strategies for a highly-stretched mesh in close proximity to non-planar geometric boundaries remain a focus of ongoing research.

The current work seeks to validate the output (adjoint) based error estimation procedure for use in near-field sonic boom pressure signature prediction. The cost function is formulated from the integral of the near-field pressure differential over a prescribed surface. This technique systematically focuses on adapting the mesh at the locations which contribute to error in the cost function. The error estimation and mesh adaptation are conducted **without** the aid of *a priori* information about the flow field structure and without the need for experienced human intervention. The method is validated here using two non-lifting geometries and has been previously shown to predict signatures for a lifting wing-body geometry.²²

II. Flow Solver

The fully unstructured Navier-Stokes three-dimensional^{23–25}(FUN3D) suite of codes is employed in this study. The compressible flow solver employs an unstructured finite-volume tetrahedral method for conserved variables, \mathbf{Q} , i.e.,

$$\mathbf{Q} = [\rho \ \rho u \ \rho v \ \rho w \ E]^T \quad (1)$$

where ρ is density, u , v , and w are velocity components, and E is total energy per unit volume. The node-based variables, \mathbf{Q} , are computed by driving the flow equation residual \mathbf{R} to steady-state with an implicit point-iterative method or an implicit line relaxation scheme.²⁶ FUN3D is able to solve incompressible and compressible formulations of the Euler and Reynolds-averaged Navier-Stokes (RANS) flow equations, either tightly or loosely coupled to the Spalart-Allmaras²⁷ (S-A) one-equation turbulence model. When the S-A model is included, the turbulence model quantity $\tilde{\nu}$ is included in \mathbf{Q} . The present study employs only the Euler equations due to the area of interest being the near-field at more than 5 body lengths. The solution of \mathbf{Q} allows the calculation of integral quantities f (e.g., lift and drag).

III. Adjoint Solver

After the flow solution is known, the discrete adjoint equations^{24,25} are solved to complete the dual problem. The first step is to linearize the flow equation residual (including the turbulence model) \mathbf{R} and output function f with respect to the flow solution \mathbf{Q} . After this linearization, an adjoint variable λ is solved for each of the flow equations and the turbulence model. An abbreviated derivation, adapted from Taylor et al.,²⁸ is given below. The chain rule for the linearized output function is

$$\frac{\partial f}{\partial \mathbf{Q}} = \left(\frac{\partial f}{\partial \mathbf{R}} \right)^T \frac{\partial \mathbf{R}}{\partial \mathbf{Q}} \quad (2)$$

The adjoint variable λ is defined as the linearized effect of a flow residual source term on the output function:

$$\frac{\partial f}{\partial \mathbf{R}} = \lambda \quad (3)$$

This set of linear equations is solved to find λ :

$$\left(\frac{\partial \mathbf{R}}{\partial \mathbf{Q}} \right)^T \lambda = \frac{\partial f}{\partial \mathbf{Q}} \quad (4)$$

Once the flow solution is known, this set of linear equations is solved with a point-iterative time-marching method or an implicit line relaxation scheme.^{26,29} To speed execution, the global problem domain is decomposed into multiple sub-domains, and the flow and the adjoint problems are solved with a parallel execution scheme, which communicates via the message passing interface (MPI) standard.

IV. Error Correction

The error prediction and correction scheme is taken from Refs. 18 and 19. With a solution on a mesh of reasonable size \mathbf{Q}^0 , it is desirable to predict the value of an output function evaluated with a solution on a much finer mesh $f(\mathbf{Q}^*)$. This prediction can be computed without the solution on this finer mesh when the adjoint solution on this reasonable mesh λ^0 is used. The full derivation of the error correction term is available in Refs. 16, 18, 19, and 17. An abbreviated derivation is presented by expanding the Taylor series about $f(\mathbf{Q}^0)$, i.e.,

$$f(\mathbf{Q}^*) = f(\mathbf{Q}^0) + \left(\frac{\partial f}{\partial \mathbf{R}} \right)^T \bigg|_0 (\mathbf{R}(\mathbf{Q}^*) - \mathbf{R}(\mathbf{Q}^0)) + \dots \quad (5)$$

Employing Eq. (3) and assuming that the residual on the much finer mesh is zero yields an improved estimate for the functional of interest f_{est} :

$$\frac{\partial f}{\partial \mathbf{R}} \bigg|_0 = \lambda^0 \quad (6)$$

$$\mathbf{R}(\mathbf{Q}^*) = 0 \quad (7)$$

$$f(\mathbf{Q}^*) \approx f_{est} = f(\mathbf{Q}^0) - (\lambda^0)^T \mathbf{R}(\mathbf{Q}^0) \quad (8)$$

To improve the prediction of the functional f_{est} , \mathbf{Q}^0 and λ^0 can be interpolated to an embedded mesh. Interpolation is performed in two ways for this study: a linear interpolation (\mathbf{Q}^L, λ^L) and a higher order interpolation (\mathbf{Q}^H, λ^H). Details of this interpolation and the construction of this embedded mesh are in Ref. 21, including special considerations required for interpolating λ for problems with strong boundary conditions.¹⁸ Substituting the higher order interpolant into Eq. (8) yields the higher order functional estimate f_{est}^H :

$$f_{est}^H = f(\mathbf{Q}^H) - (\lambda^H)^T \mathbf{R}(\mathbf{Q}^H) \quad (9)$$

V. Adaptation Parameter

The adaptation parameter, also from Ref. 18 and 19, is intended to specify a mesh spacing modification to reduce the uncertainty in the computed error prediction. The mesh is not modified to directly reduce the computed error prediction (as in Ref. 17) because an accurate estimate for the functional, including this error term, can be computed with Eq. (8). Instead, targeting the uncertainty in this computed quantity is more effective and improves the robustness of the adaptive process. The error correction (Eq. (8)), including the uncertainty in the dual solution, is

$$f(\mathbf{Q}^0) - f(\mathbf{Q}^*) \approx (\lambda^0)^T \mathbf{R}(\mathbf{Q}^0) + (\lambda^* - \lambda^0)^T \mathbf{R}(\mathbf{Q}^0) \quad (10)$$

The uncertainty in the computed error correction is

$$f_{est} - f(\mathbf{Q}^*) \approx (\lambda^* - \lambda^0)^T \mathbf{R}(\mathbf{Q}^0) \quad (11)$$

The relation of the primal and dual problems^{16,18,19} yields another expression for the error correction uncertainty

$$(\lambda^* - \lambda^0)^T \mathbf{R}(\mathbf{Q}^0) = \mathbf{R}_\lambda(\lambda^0)(\mathbf{Q}^* - \mathbf{Q}^0)^T \quad (12)$$

where $\mathbf{R}_\lambda(\lambda)$ is the residual of the dual problem:

$$\mathbf{R}_\lambda(\lambda) = \left(\frac{\partial \mathbf{R}}{\partial \mathbf{Q}} \right)^T \lambda - \left(\frac{\partial f}{\partial \mathbf{Q}} \right)^T \quad (13)$$

A computable term is found by using the interpolation error of λ to replace $(\lambda^* - \lambda^0)$, and the interpolation error of \mathbf{Q} to replace $(\mathbf{Q}^* - \mathbf{Q}^0)$. The higher order interpolant for \mathbf{Q}^0 and λ^0 is employed for the residual calculations to improve prediction in place of the linear interpolant in Ref. 18 and 19. The linear interpolant yields a more conservative estimate of the remaining error; the high-order interpolant generally results in a more accurate estimate of the remaining error on the final adapted mesh. The high-order interpolant estimate may underestimate the remaining error on very coarse initial meshes, but the estimation improves as the adaptation process proceeds. The interpolation error is expressed as the difference in the high-order and linear interpolated values:

$$(\lambda^* - \lambda^0) \approx (\lambda^H - \lambda^L) \quad (14)$$

$$(\mathbf{Q}^* - \mathbf{Q}^0) \approx (\mathbf{Q}^H - \mathbf{Q}^L) \quad (15)$$

The average of the absolute values of the two uncertainty terms in Eq. (12) yields the adaptation intensity \mathbf{I} , which is computed for each equation on each embedded node:

$$\mathbf{I} = \frac{|(\lambda^H - \lambda^L)^T \mathbf{R}(\mathbf{Q}^H)| + |\mathbf{R}_\lambda(\lambda^H)(\mathbf{Q}^H - \mathbf{Q}^L)^T|}{2} \quad (16)$$

The intensity \mathbf{I} is therefore the average of the absolute values of two terms. The first term is a dual solution interpolation error weighted with the primal residual. The second term is the a primal solution interpolation error weighted with the dual problem residual. This form of the adaptation intensity (which includes weighed interpolation errors) focuses on the nonlinear contributions to the function error, which increases robustness of the adaptation method. The global sum of the adaptation parameter (Eq. 16) can be used also as an estimate of the error remaining after the error correction term is applied. Reference 21 details how \mathbf{I} is combined with a user-specified output error tolerance and Mach Hessian

to compute an anisotropic metric specification. In the current work, the element anisotropy is limited to 20:1. This constraint was selected for robustness near curved boundaries; removing such limitations is the focus of ongoing research.

VI. Error Correction and Adaptation Process

The error correction process begins with an initial tetrahedral mesh, which can come from any mesh generation system. This initial mesh is partitioned to allow parallel execution. The state variables are computed in parallel as the nonlinear solution to the flow equations on the initial mesh, and then the adjoint variables are computed also in parallel with the linearized field equations about the converged flow solution. To compute the error prediction and the adaptation parameter, a globally embedded, or h-refined mesh, is created with interpolated primal and dual solutions. In the previous work of Ref. 21, the global problem domain was reconstructed to facilitate the creation of a finer, embedded mesh with interpolated primal and dual solutions. However, in the current work, the computation of the error prediction and the adaptation parameter has been implemented with a parallel execution scheme. Once the adaptation parameter for a given mesh has been computed, this parameter can be used to specify an isotropic or anisotropic adaptation metric to a suite of mesh adaptation modules that also have a distributed memory, parallel execution scheme.^{21,30} The FUN3D suite of codes is able to directly interface with the adaptation modules to avoid disk operations that can be costly on commodity clusters.

The adaptation modules use local mesh operators to remove edges by collapsing those that are too small as compared to the specified anisotropic metric. Edges that are too long as compared to the specified anisotropic metric are split. Grid element quality is improved by swapping edges to new configurations. Node locations are also smoothed to improve the quality of the worst incident element. This smoothing is performed in the interior and on the boundary of the domain. The new nodes that are inserted by an edge split on the boundary are moved to the correct position on a high fidelity boundary representation with a global linear elasticity mesh movement scheme. The interface with high fidelity boundary representation is facilitated by the GridEx^{31,32} framework.

The GridEx framework is currently being developed to link various mesh generation and adaptation strategies to geometry through the Computational Analysis Programming Interface^{33–35} (CAPRI). CAPRI is a CAD vendor-neutral package that provides a common interface to many native CAD kernel application programming interfaces (API). Interrogating CAD parts with their native kernel removes the difficulties of translation and associated pitfalls. The GridEx framework utilizes CAPRI to store the discretized edge and face parameters. The framework also augments the underlying CAD geometry kernels to improve the robustness of surface parameter resolution. While the actual CAD solid model is preferred, the adaptation modules provide a method of specifying analytical surface geometry. This surrogate geometry source allows the adaptation of meshes that lack the discretized edge and face parameters of a CAD solid model.

For inviscid meshes and applications, both anisotropic surface and field adaptation can be prescribed. As in Ref. 21, the mechanics to automatically adapt 3-D meshes with highly anisotropic regions near curved boundaries is still underway. Therefore, in high Reynolds number viscous cases, the mesh can only be automatically adapted in the field outside of the advancing layer structure.

VII. Sonic Boom Cost Function

The goal is to reduce the uncertainty of a calculated pressure signal in the near-field of the target configuration. The pressure signal is a non-dimensional quantity defined by

$$g(\mathbf{x}) = \frac{\Delta p(\mathbf{x})}{p} \quad (17)$$

where Δp is the difference between the local and free-stream static pressure.

A scalar objective function f is formulated by integrating Eq. (17)

$$f = \iint g \, dA \quad (18)$$

over a cylindrical surface with a radius equal to the near-field distance from the body where the pressure signature is desired. This distance is typically non-dimensionalized by a reference body length, l . The cylindrical integration surface may also be limited to a specific area of interest. In the current work, the surface extends slightly ahead of

and behind the expected shocks and is limited to a small distance off the symmetry plane to simulate the 1-D nature of experimental measurements.

The output function formulation, while sufficient for reducing the uncertainty in the calculated pressure signal, does not provide an intuitive means of specifying an absolute error tolerance. In contrast to a drag-based output function where the tolerance can be defined from experience, say ± 1 count. There is insufficient experience to judge how accurately the signal must be resolved for satisfactory propagation to the ground. For the purposes of this study, the acceptable tolerance was lowered repeatedly until the mesh was refined to the point where the computational hardware being used became the limiting factor. All cases were executed on an Intel Linux cluster of 12 compute nodes each with 1.5GB of RAM. The computed estimation of the remaining error from Section V is monitored relative to the magnitude of the cost function as a measure of convergence.

VIII. Computational Results

Primary validation of the method has been conducted with a test matrix of axisymmetric cone-cylinder models for which test data has been established. Reference 36 was used to provide reference data for the adaptively enhanced CFD calculations. The reference body length for the articles in this study was 2 inches and matches the definition from Ref. 36. A cylinder was fixed to the base of each model and extended 15 inches downstream. A conical computational domain for the CFD calculations was defined with the inlet plane at 55° and the exit plane at 25° so as to exceed the Mach lines characteristic of the upper and lower test conditions. The exit plane was extended to a height of 60 inches. All computations were run at 0° angle-of-attack.

A. Cone-Cylinder Configuration

Model 1 of Ref. 36 represents a 3.23° cone cylinder. The cone has 2 inch length and a radius governed by,

$$r = x \sqrt{\frac{0.01}{\pi}} \quad (0 \leq x \leq l) \quad (19)$$

For this study the geometry model was re-created from the analytical description given in Ref. 36 using the Unigraphics CAD system. The model was given a 0.003 inch radius at the nose to simulate the wind tunnel model. To minimize computational costs, the computational domain about the axisymmetric model was defined as a 9.0° wedge as measured from the symmetry plane. A baseline mesh of 6230 nodes was constructed with GridEx based on crude refinement near the surface. No consideration was given to the existence of shocks nor to other flow field considerations. It should be emphasized that no *a priori* knowledge of the test data has been used in the initial mesh generation nor the adaptation process. Instead, the baseline mesh was generated and used to seed an automated, iterative procedure which consists of flow field and corresponding adjoint solutions, error estimates, and finally mesh adaptation all in a parallel environment. An adapted mesh for $M = 1.26$ consisting of 700,000 nodes resulted following 17 such cycles. For $M = 1.41$, a mesh of 727,000 nodes was produced after 15 adaptation cycles. The cost function was evaluated over a 0.1 inch wide strip between stations $X = 20.0$ and $X = 80.0$ of the cylindrical integration surface. The surface was placed in the field at $h/l = 18$ for the $M = 1.26$ condition and at $h/l = 20$ for $M = 1.41$.

The pressure signatures at various distances from 5 to 20 body lengths are plotted in Figure 1 for the axisymmetric flow fields at $M = 1.26$ and $M = 1.41$ conditions. The FUN3D pressure signatures were extracted from the adapted mesh solution along the body centerline (symmetry plane). The data is presented in the same parametric form as used in Ref. 36 such that it is in accordance with theoretical considerations of that report. Please note that the experimental data was digitized by hand from a copy of Fig. 4 (a) on page 13 of Ref. 36. Very good agreement is observed not only at the considerable h/l locations of 18 and 20 where the cost function was evaluated, but also at the intermediate h/l locations. This behavior is believed to be specific to the sonic boom application due to the propagation of errors in the cost function along characteristics. Though not detailed in this report, a separate adaptation study was conducted with the cost function integration surface directly at $h/l = 6$ and $h/l = 10$ for the $M = 1.26$ condition. Negligible difference was observed in the pressure signatures for this model with collocated integration surfaces.

The mesh adaptation process is demonstrated in Figure 2 for the $M = 1.26$ test case. Shown in Figure 2 (a) is the baseline mesh on the symmetry plane along with the corresponding plot of the pressure signature at the maximum $h/l = 18$ near-field distance shown in Figure 1 for convenient reference. The $h/l = 18$ location is represented by the black horizontal line through the mesh. It should be noted that the solution on this baseline mesh yields essentially a

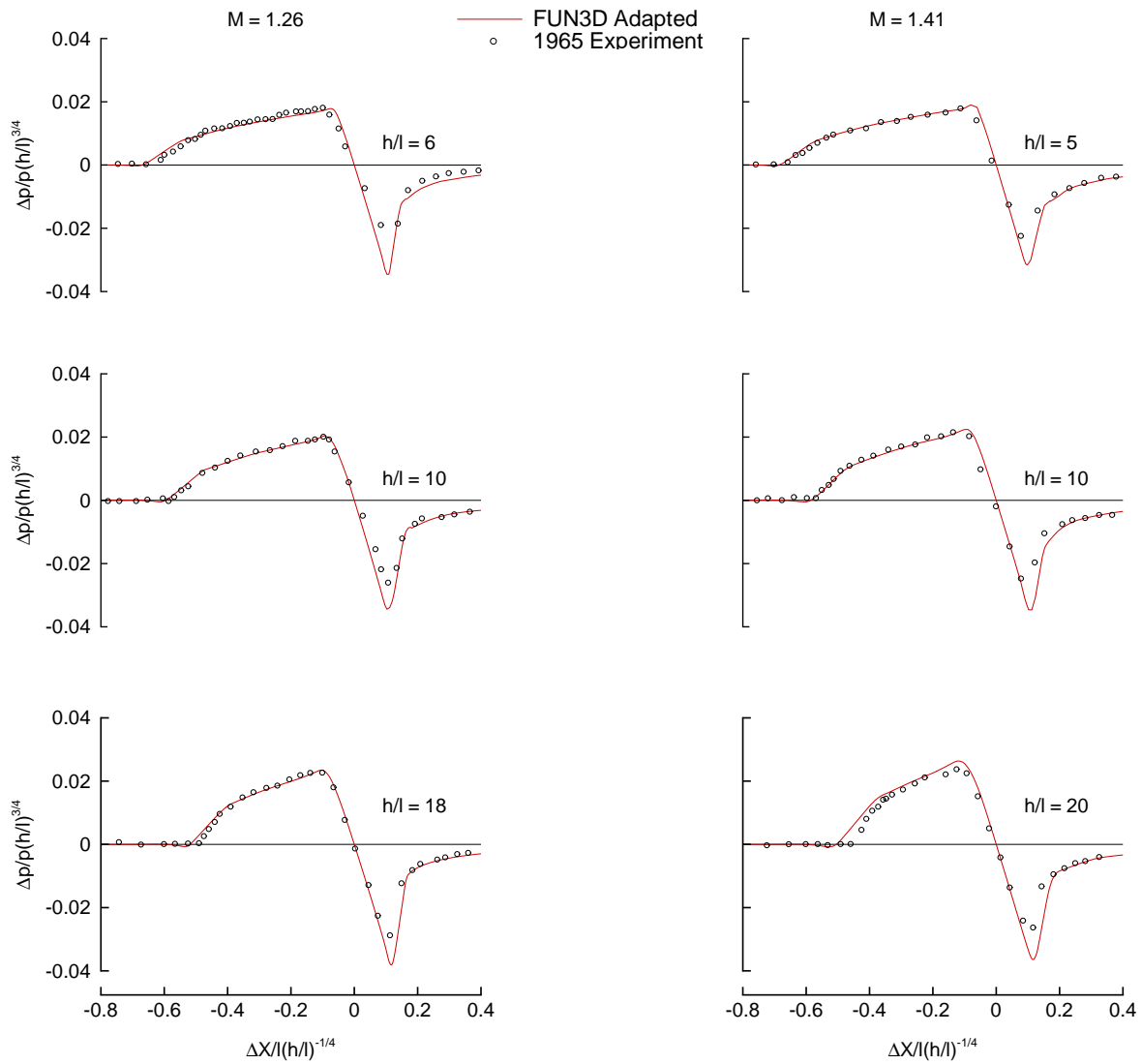


Figure 1. Comparison of FUN3D Adapted Mesh Solution and Experiment.

zero pressure differential at the near-field location of interest indicating the absence of shock wave propagation into the field. Though not shown in the figure, the signature is also only minimally perturbed at $h/l = 6$ and $h/l = 10$ distances for the solution on this crude initial mesh.

Figure 2 (b) shows the solution that results from the adapted mesh under the same conditions. Recall from Fig 1 that very good agreement with experiment is observed at all measurement locations. The data of Fig 1 for $M = 1.26$ was extracted from the solution of Fig. 2 (b).

Similarly, the initial and adapted mesh and solution for the $M = 1.41$ condition are represented in Figure 3. The corresponding data at $h/l = 20$ from Figure 1 is again included for reference. The same initial mesh was used to start the process and yields the same unacceptable solution of Figure 3 (a). Note again the lack of shock wave propagation in this solution. The adapted mesh results in the solution seen in Figure 3 (b) for $M = 1.41$. It is this adapted mesh that is the source of the very good agreement of data of Figure 1 even at large distances from the body.

Interesting anomalies apparent in Figs. 2 (b) and 3 (b) should be noted. First, the mesh refinement which occurs toward the aft end of the cylinder is not well understood at this time. The reason for this behavior may be an artifact of the outflow boundary condition, although efforts to mitigate this effect have been unsuccessful to date. Also, because the geometry at the cone-cylinder surface is resolved using triangular elements, a number of small spurious shocks appear immediately adjacent to the geometry. These artificial features are often targeted for refinement by successive iterations of the adaptation procedure, during which the features tend to disappear. As the minimal impact of these spurious flow features on the cost function become evident, the procedure subsequently strives to coarsen in these regions, leading to a repetitive cycle of refinement and coarsening. Strategies aimed at minimizing this effect are underway.

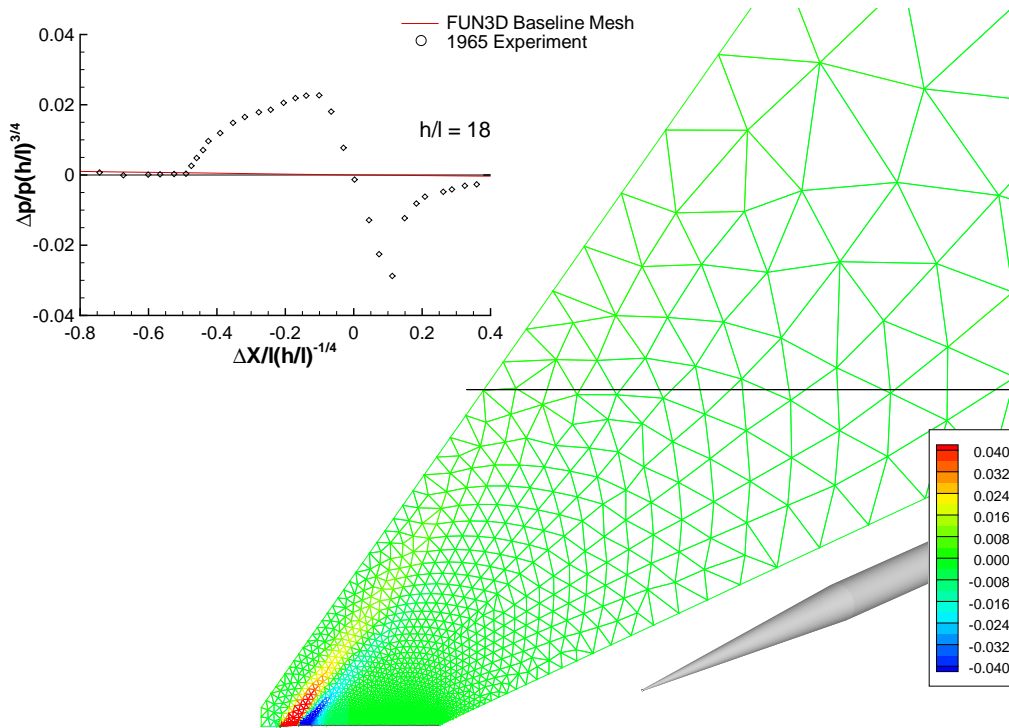
As mentioned earlier, the specification of the error tolerance that controls the computation of anisotropic adaptation metric is not as intuitive for the sonic boom cost function as it is for true force calculations such as lift or drag. However, a reasonable tolerance can be estimated by examining the estimated error remaining from a previous cycle. In addition, it is common practice to schedule predetermined reductions in the tolerance. This is due in part to the large solution errors in the early stages of adaptation that result from the crude initial mesh. Scheduled reduction of the error tolerance allows for a gradual improvement of the mesh and solution with each adaptation cycle. Given that the tolerance is based on the calculated error estimation, the schedule is not based on *a priori* knowledge of the flow field. Both of these practices were applied throughout this study without compromising the process automation.

Figures 4 and 5 plot the convergence of the sonic boom cost function as a function of mesh size. Included in the plots are error bars that represent the computed estimate of the remaining error in the cost function for each mesh. Note that the initial mesh was omitted from these plots as the large error bars from the baseline solution required a scaling of the ordinate that washes out more relevant features of subsequent meshes. Also, once the remaining error estimate falls below a given error tolerance, the mesh adaptation procedure has little if any affect. In this regard the process is viewed as self-terminating. However, since the error tolerance scheduling is predetermined, the remaining error of some cycles may in fact already be below the current tolerance value. The result is little, primarily superficial, alteration of the mesh. These cases would essentially over plot existing data and have been omitted here for clarity. Note that the initial convergence is not necessarily monotonic. Close inspection of Figures 4 and 5 reveals that the initial adaptation steps may over refine the mesh with considerable error remaining. Succeeding steps in the process, which coincidentally may be accompanied by a tolerance reduction, may actually coarsen the mesh while reducing the global error. This is not surprising considering the coarseness of the initial mesh and the large error associated with its solution. The early adaptation cycles have yet to establish asymptotic convergence of the cost function. The robustness of the process however quickly establishes a stable refinement sequence.

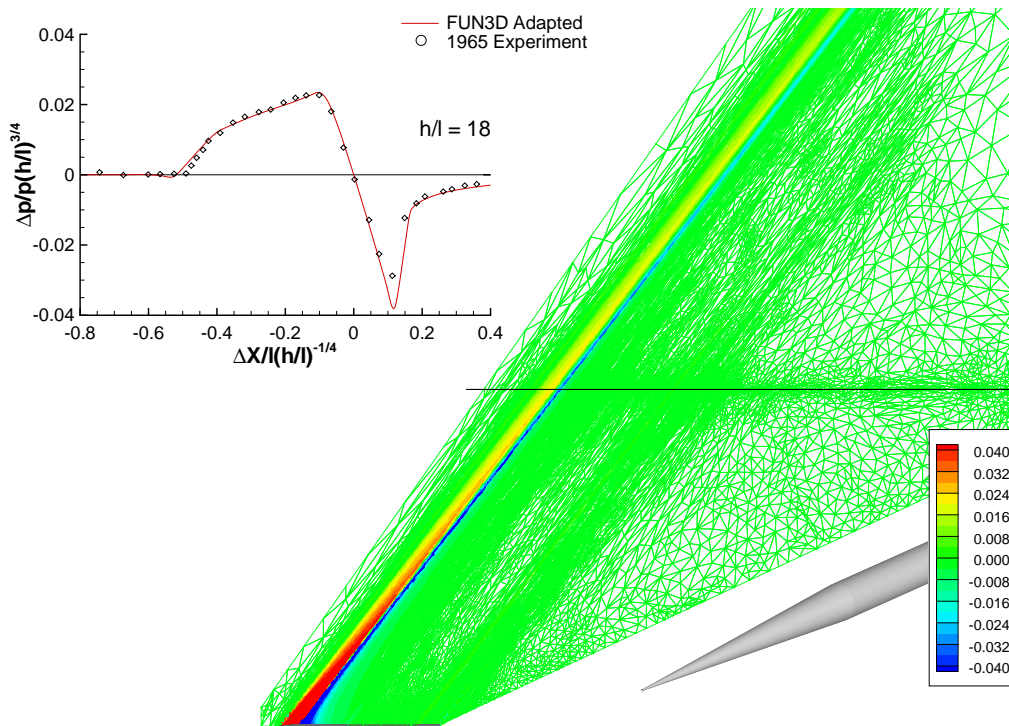
We see from Figures 4 and 5 that as the function converges so does the error estimate as indicated by the error bars. Also, as the remaining error converges, the accuracy of the pressure signature improves as would be expected (see figure insets). The extent of these adaptation cycles is somewhat academic since the final error tolerance is not predetermined for this cost function. Examination of these plots indicates that sufficient convergence of the cost function most likely occurred one to two cycles earlier than the final mesh result. While the final mesh had roughly 700,000 nodes, a mesh of roughly one third its size can potentially produce an acceptable signature (as indicated by the outlined inset). The error bounds provide a means of evaluating and substantiating the accuracy based on the intended application of the pressure signatures.

B. Double-Cone Sonic Boom Configuration

Model 8 of Ref. 36 was also selected for validation of the the adjoint-based error estimation and adaptation method. This model represents two tandem cones connected by a cylinder subjected to 3-D Mach 1.26 and Mach 1.41 inviscid flows at 0.0° angle of attack. The model is defined analytically by Ref. 36 as,

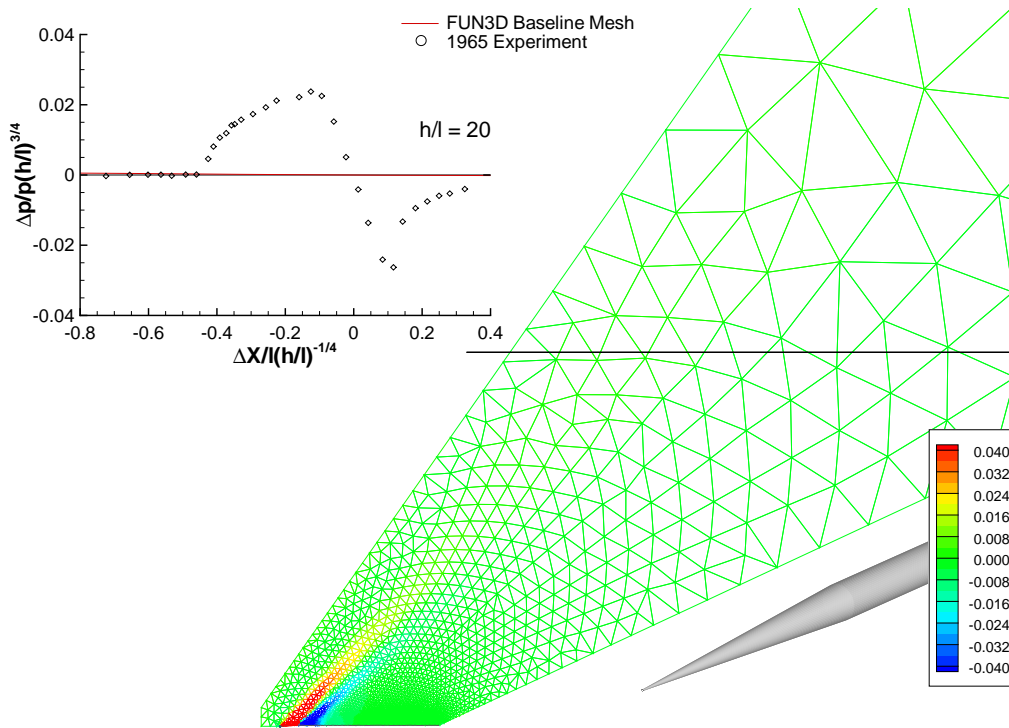


(a) Baseline mesh and solution

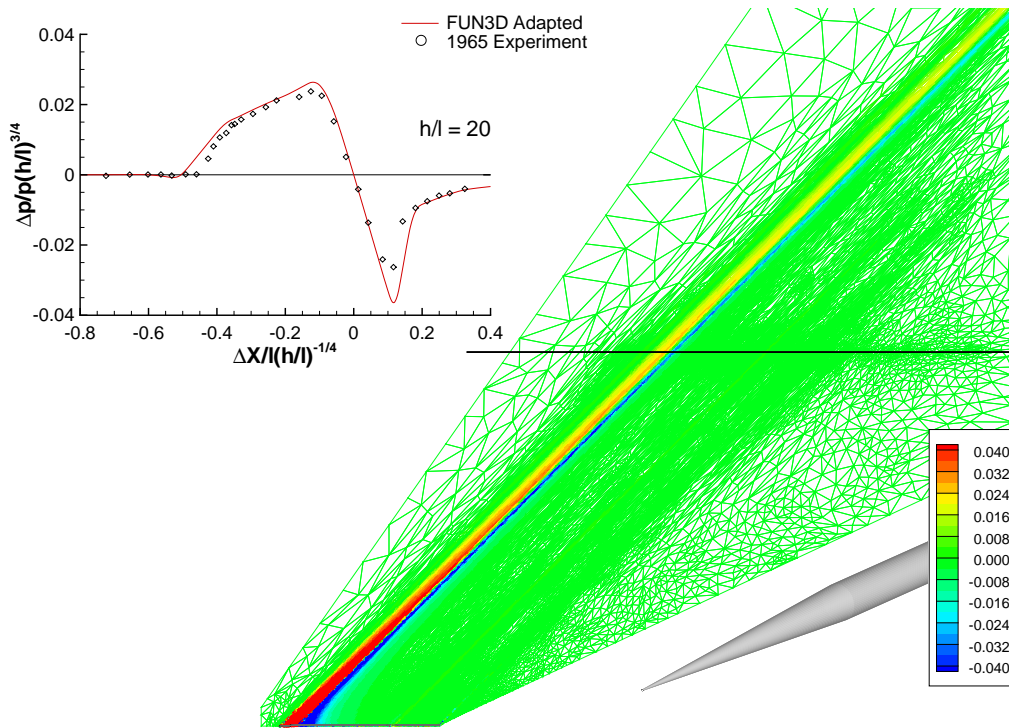


(b) Adapted mesh and solution

Figure 2. Mesh Adaptation, Cone-Cylinder Test Article, $M = 1.26$.



(a) Baseline mesh and solution



(b) Adapted mesh and solution

Figure 3. Mesh Adaptation, Cone-Cylinder Test Article, $M = 1.41$.

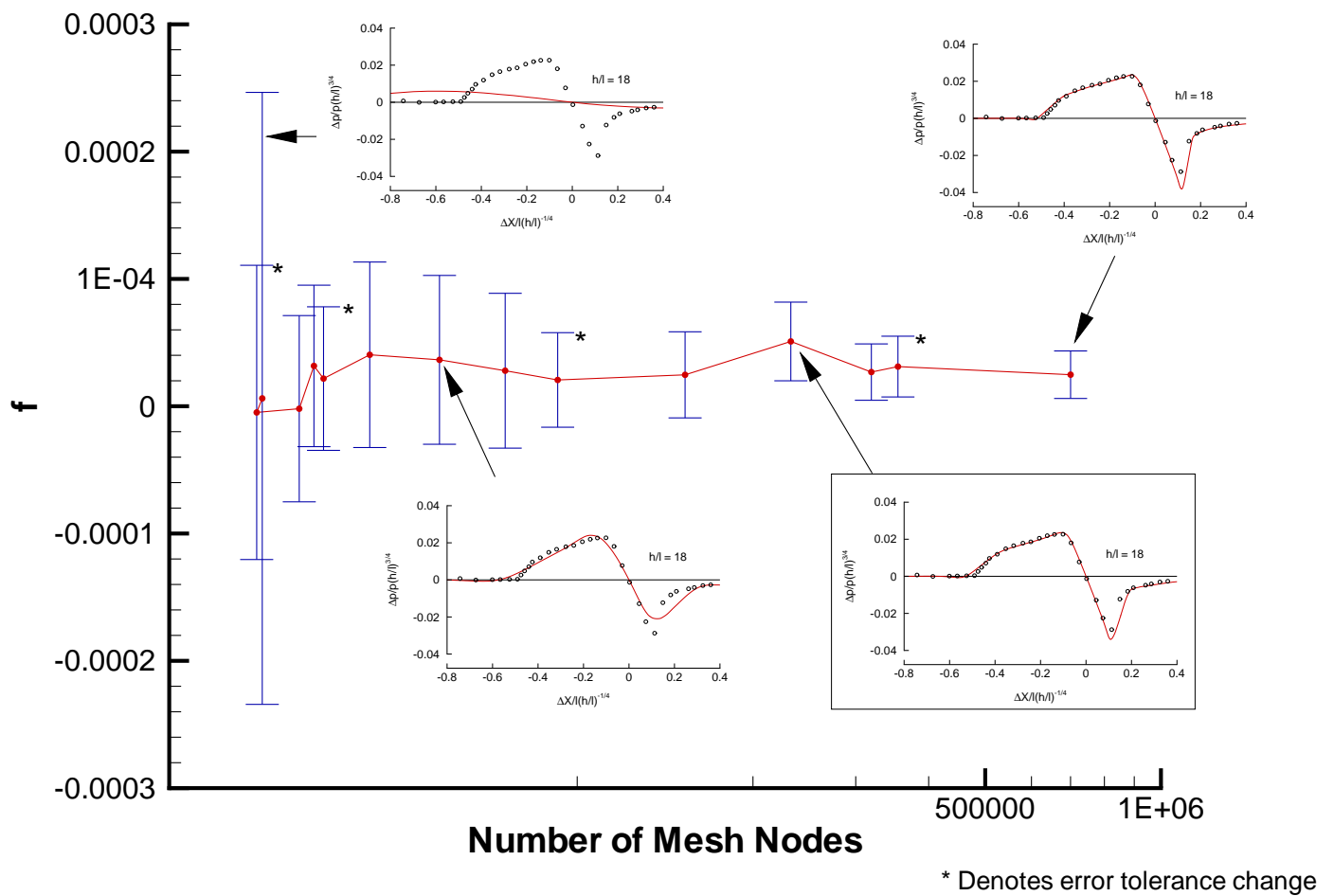


Figure 4. Cone-Cylinder Cost Function Convergence $M = 1.26$.

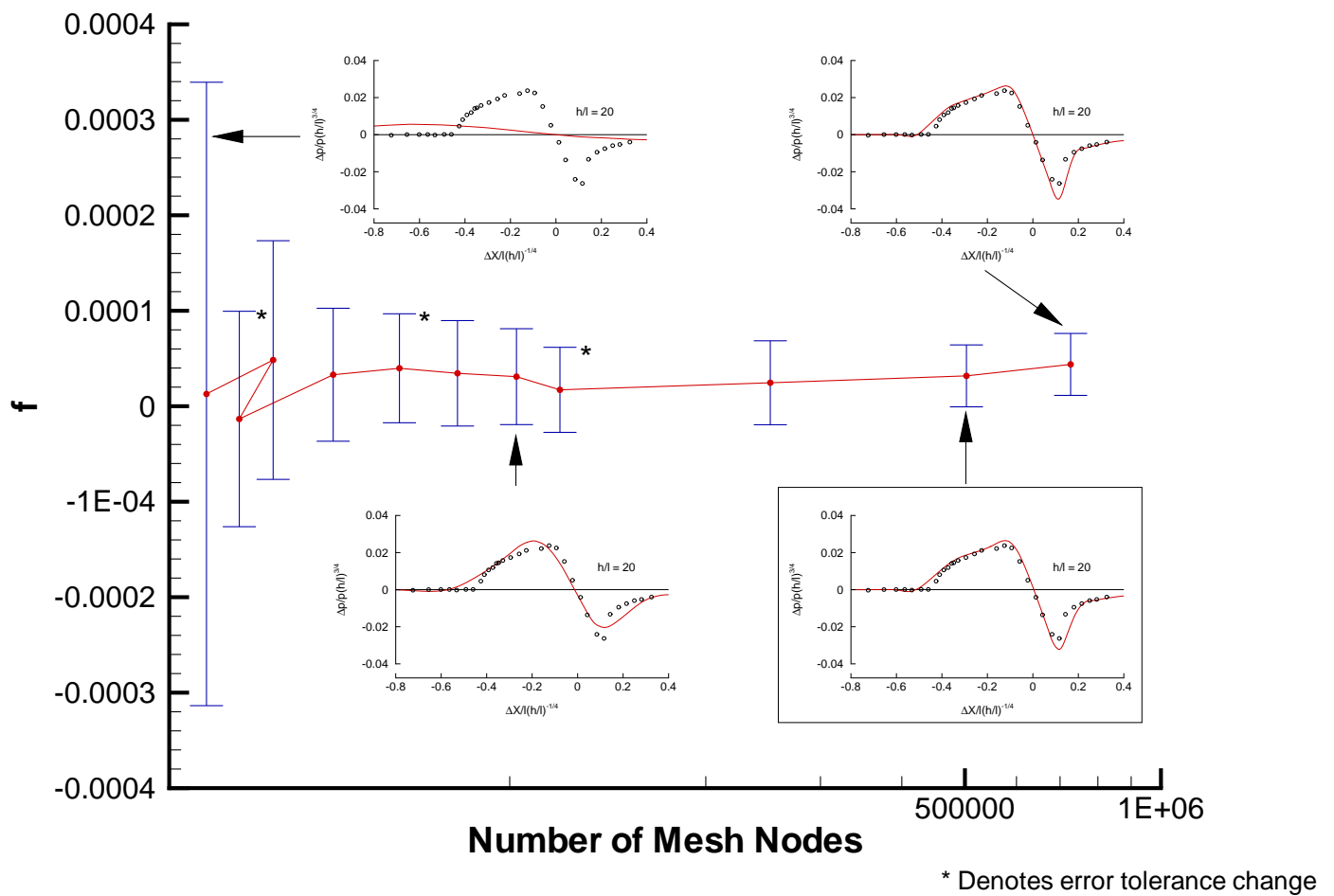


Figure 5. Cone-Cylinder Cost Function Convergence $M = 1.41$.

$$r = x \sqrt{\frac{0.08}{\pi}} \quad (0 \leq x \leq 0.25l) \quad (20)$$

$$r = \sqrt{\frac{0.02}{\pi}} \quad (0.25l \leq x \leq 0.75l) \quad (21)$$

$$r = \frac{2}{2 + \sqrt{2}} \sqrt{\frac{0.04}{\pi}} \left(x - \frac{2 - \sqrt{2}}{2} \right) \quad (0.75l \leq x \leq l) \quad (22)$$

The geometry model was re-created from the analytical description using the Unigraphics CAD system with a 0.003 inch radius at the nose as in the cone-cylinder case. The domain was defined similarly to that of the cone-cylinder model and limited to the 9.0° wedge. A baseline mesh of 4400 nodes was constructed using GridEx. An adapted mesh for the $M = 1.26$ condition was generated consisting of 400,000 nodes following 20 cycles of adaptation. The $M = 1.41$ condition resulted in a mesh of 742,000 nodes after 22 adaptation cycles. The difference in mesh size can be attributed to different definitions for the cost function integration surface at each condition as described below.

Just as for the cone-cylinder model, the pressure signatures at various distances from 5 to 20 body lengths are plotted in Figure 6 against the experimental data of Ref. 36. Plots are included for both Mach numbers. The experimental data was sampled from Fig. 4 (h) on page 20 of Ref. 36. The FUN3D pressure signatures were extracted from the adapted mesh solutions. The cost function was again evaluated on a 0.1 inch wide integration surface at $h/l = 18$ and $h/l = 20$ for the $M = 1.26$ and $M = 1.41$ conditions respectively. However, the integration surface for this model was limited to a region from stations $X = 25.0$ to $X = 40.0$ for $M = 1.26$ and from $X = 25.0$ to $X = 50.0$ for $M = 1.41$. The difference in the length between the two conditions accounts for the different h/l and the inclination of the shock waves. The reductions in extent overall were primarily aimed at mesh efficiency. By reducing the length of the integration surface to that required of the desired pressure signature, we reduce the influence the downstream areas on the resulting cost function. This results in a reduced need to adapt those regions and yields a more efficient mesh tailored to reducing the uncertainty in the pressure signature over the limited region of interest. We also lessen the importance of the outflow boundary on the cost function and reduce the generation of the anomalies described above at the outflow boundary.

The agreement with experimental data in Figure 6 is again very good. Even subtle artifacts at the $h/l = 6$ and $h/l = 5$ locations are detected. Computed data at $h/l = 10$ is least agreeable with experiment, but as noted, the cost function was evaluated at the maximum h/l for each condition. It is expected that evaluation of the cost function at $h/l = 10$ would provide a better match if greater accuracy at that location were desired. Also some inconsistencies in the experimental data at $h/l = 10$ are observed. The definition of ΔX would imply that the experimental data should cross the abscissa with a $\Delta p/p = 0$ at $\Delta X = 0$. This is clearly not the case for the experimental data. To impose this condition, a noticeable shift of the data to the right is required for the $M = 1.41$ condition. Such a shift would improve the agreement, but has not been applied here. The discrepancy appears in the original report and is not an artifact of digitization.

The initial mesh and associated pressure differential on the symmetry plane for $M = 1.26$ are shown in Fig. 7 (a). The solid black line through the mesh indicates the location of the integration surface at $h/l = 18$. The pressure signature at this location is included for reference. As in the cone-cylinder case, the crude initial mesh fails to propagate the shock waves into the near-field as shown by the essentially zero pressure differential at the measurement location. Again, the signatures at both $h/l = 6$ and $h/l = 10$ are only minimally perturbed though not shown in this plot. The resulting symmetry plane mesh and associated non-dimensional pressure distribution after 17 cycles of error estimation and adaptation are shown in Fig. 7 (b). The final mesh has approximately 400,000 nodes.

The initial and adapted mesh and solution for the $M = 1.41$ condition are represented in Figure 8. The black line through the mesh represents the $h/l = 20$ measurement location and the corresponding data from Figure 6 is again included for reference. The same initial mesh as for $M = 1.26$ was used to start the process and yields a similar, unacceptable solution as can be seen in Figure 8 (a). Following 22 cycles of automated adaptation, the mesh of roughly 742,000 nodes and its solution are produced as shown in Figure 8 (b). The very good agreement of Figure 6 was obtained from this mesh and solution.

For these computations, the second-order reconstructions for the inviscid fluxes are not limited. The overshoots and undershoots shown near the shocks in Figures 6, 7 (b), and 8 (b) are thought to be due to this unlimited reconstruction. This is a focus of continued work and research.

Finally, Figures 9 and 10 plot the convergence of the sonic boom cost function as a function of mesh size for the Double-Cone cases. Error bars are again included to represent the computed estimate of the remaining error in the

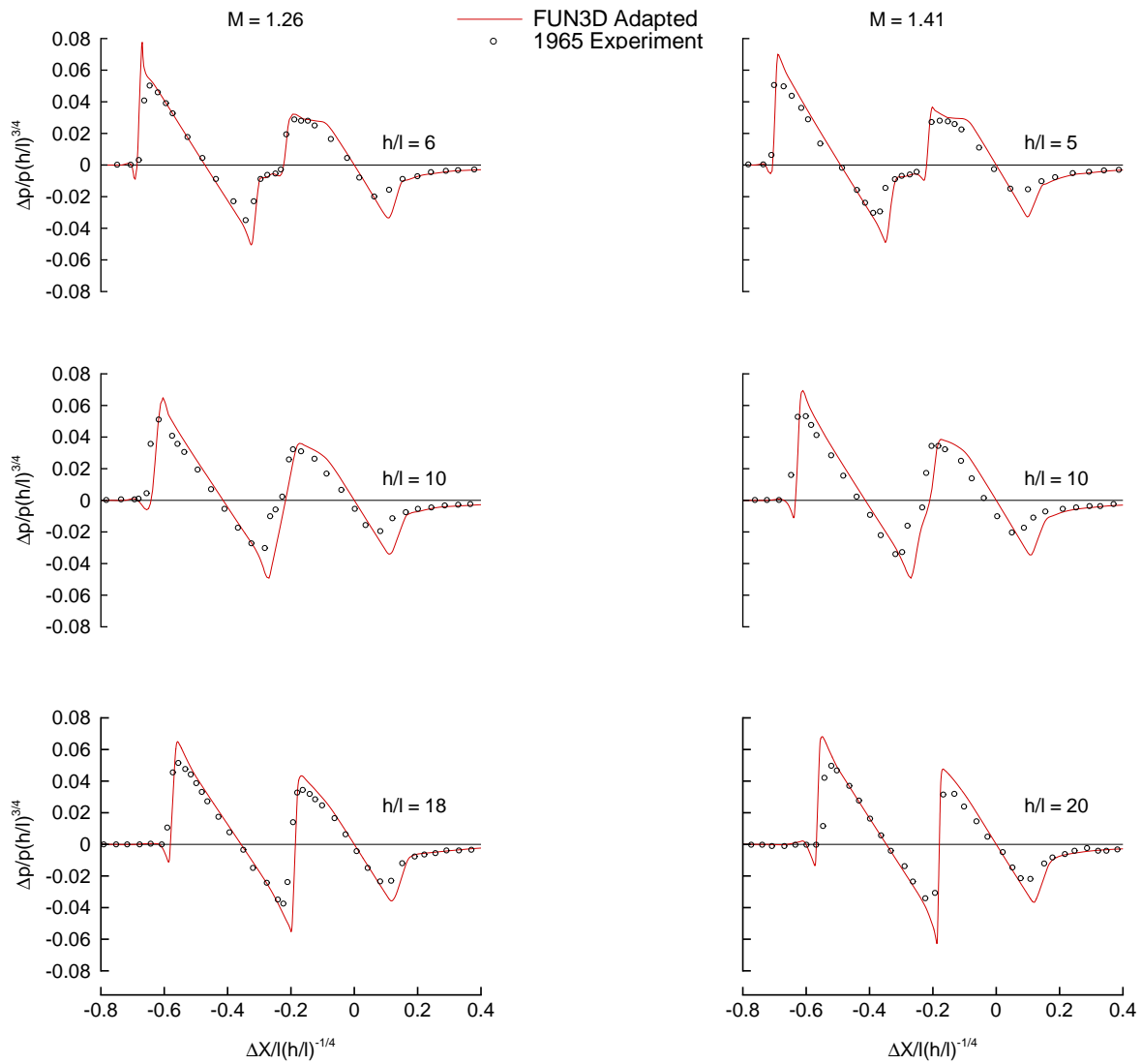
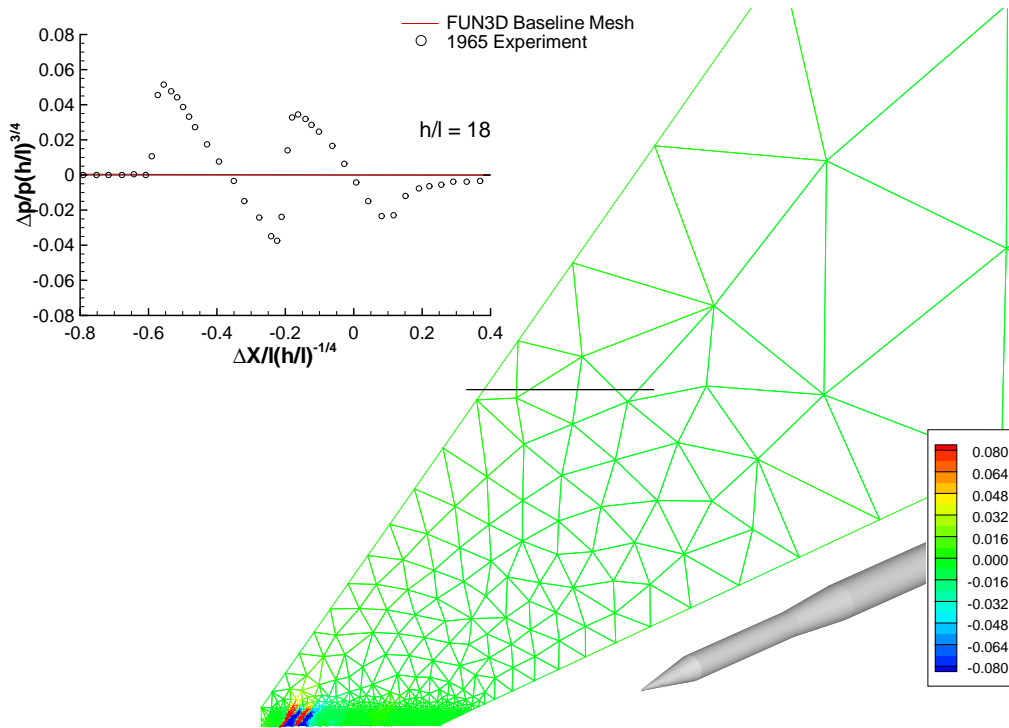
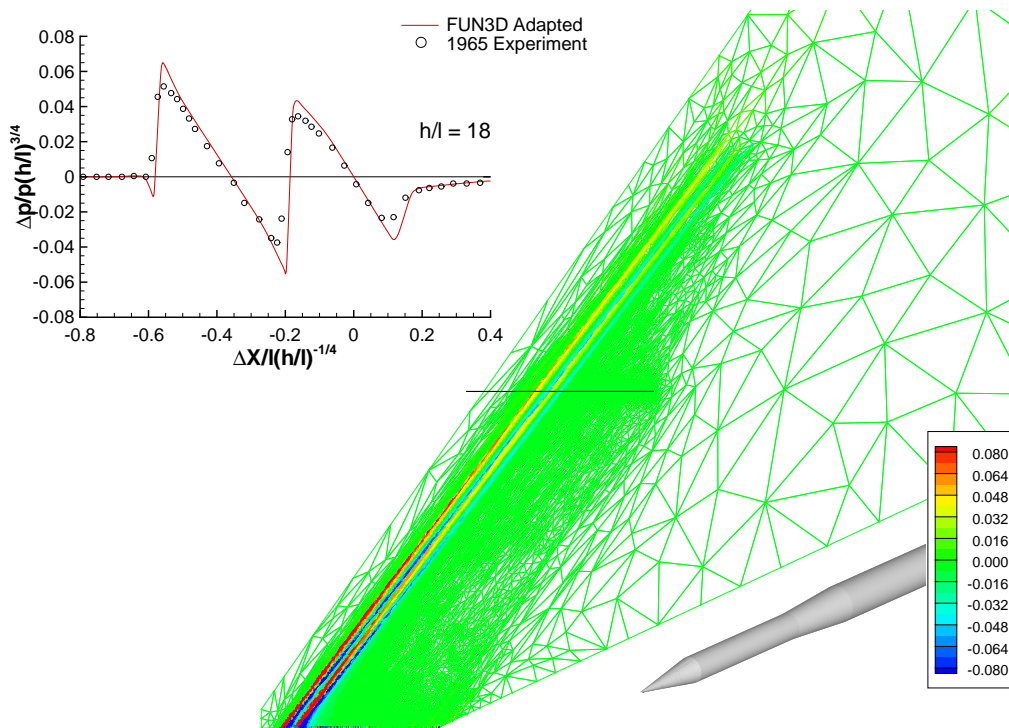


Figure 6. Comparison of FUN3D Adapted Mesh Solution and Experiment for Double-Cone.

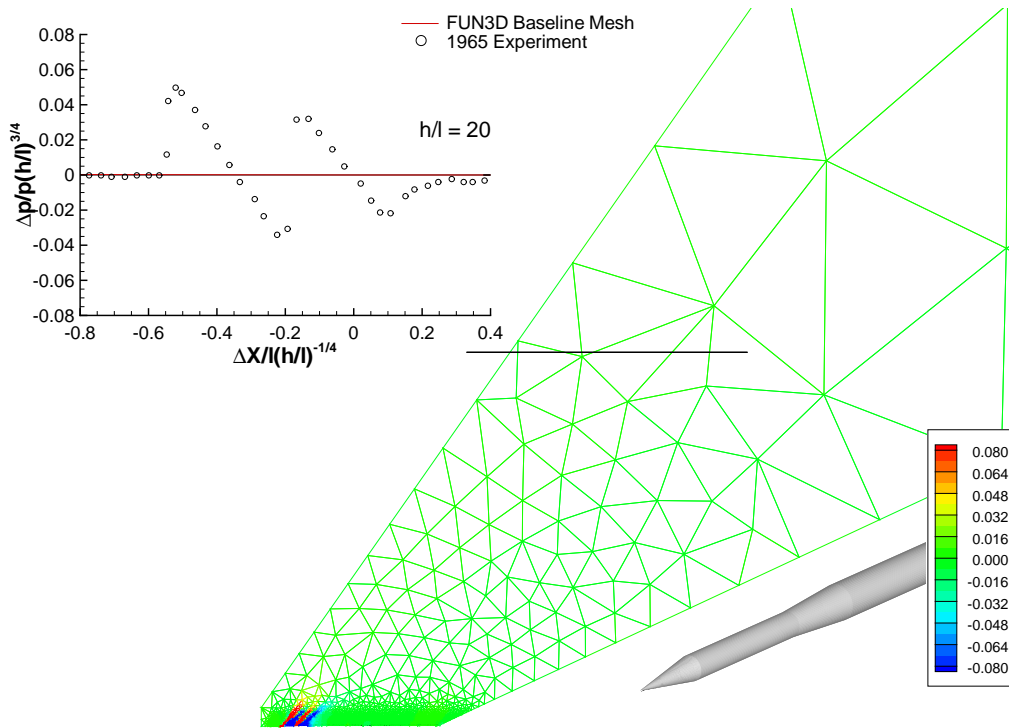


(a) Baseline mesh and solution

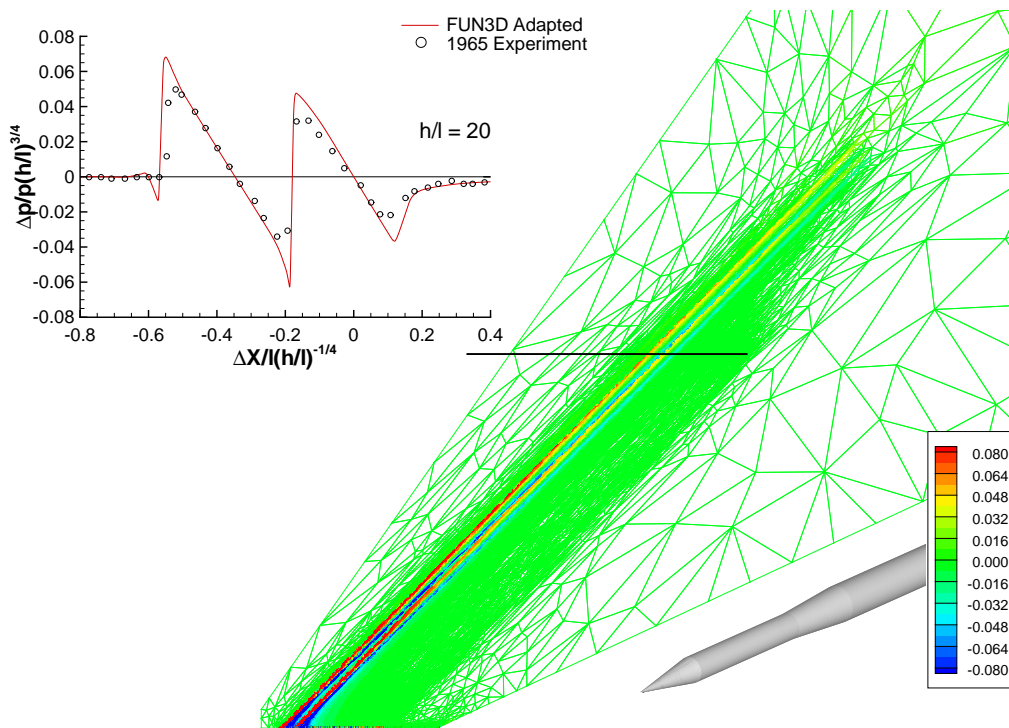


(b) Adapted mesh and solution

Figure 7. Mesh Adaptation, Double-Cone Test Article, $M = 1.26$.



(a) Baseline mesh and solution



(b) Adapted mesh and solution

Figure 8. Mesh Adaptation, Double-Cone Test Article, $M = 1.41$.

cost function for the solution on each mesh. These plots do omit the initial mesh due to the comparatively large error resulting from the initial mesh and solution. Cycles with error falling below the error tolerance are also omitted for clarity. At both conditions, the first adaptation cycle over refines the mesh, but observe that the process quickly hones in on the right course of adaptation toward a stable refinement sequence. As with the Cone-Cylinder model, observe from Figures 9 and 10 that as the function converges so does the error estimate. The error bounds provide a means of evaluating and determining the level of accuracy required based the proposed use of the pressure signatures.

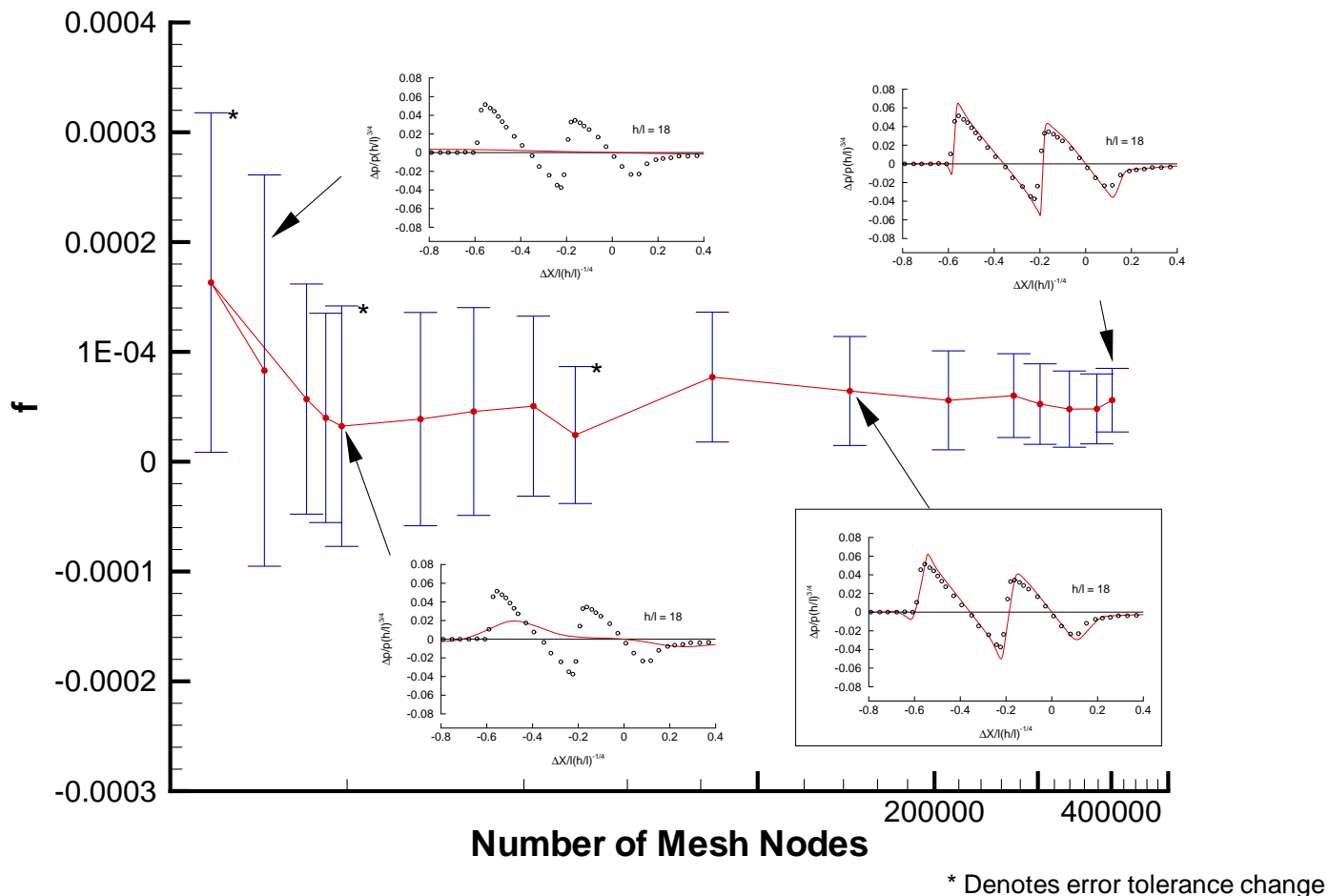


Figure 9. Double-Cone Cost Function Convergence $M = 1.26$.

IX. Summary and Discussion

The validation of an adjoint based error estimation and mesh adaptation scheme for use in the computation of near-field sonic boom pressure signatures was presented. The method seeks to reduce the uncertainty in a given cost function formulated through the integration of the pressure differential over a cylindrical surface defined in the near-field. The adjoint based approach is used to drive the cost function error estimation which in turn is used to reduce discretization error through mesh adaptation. Quantifiable error bounds on the cost function are computed that can be

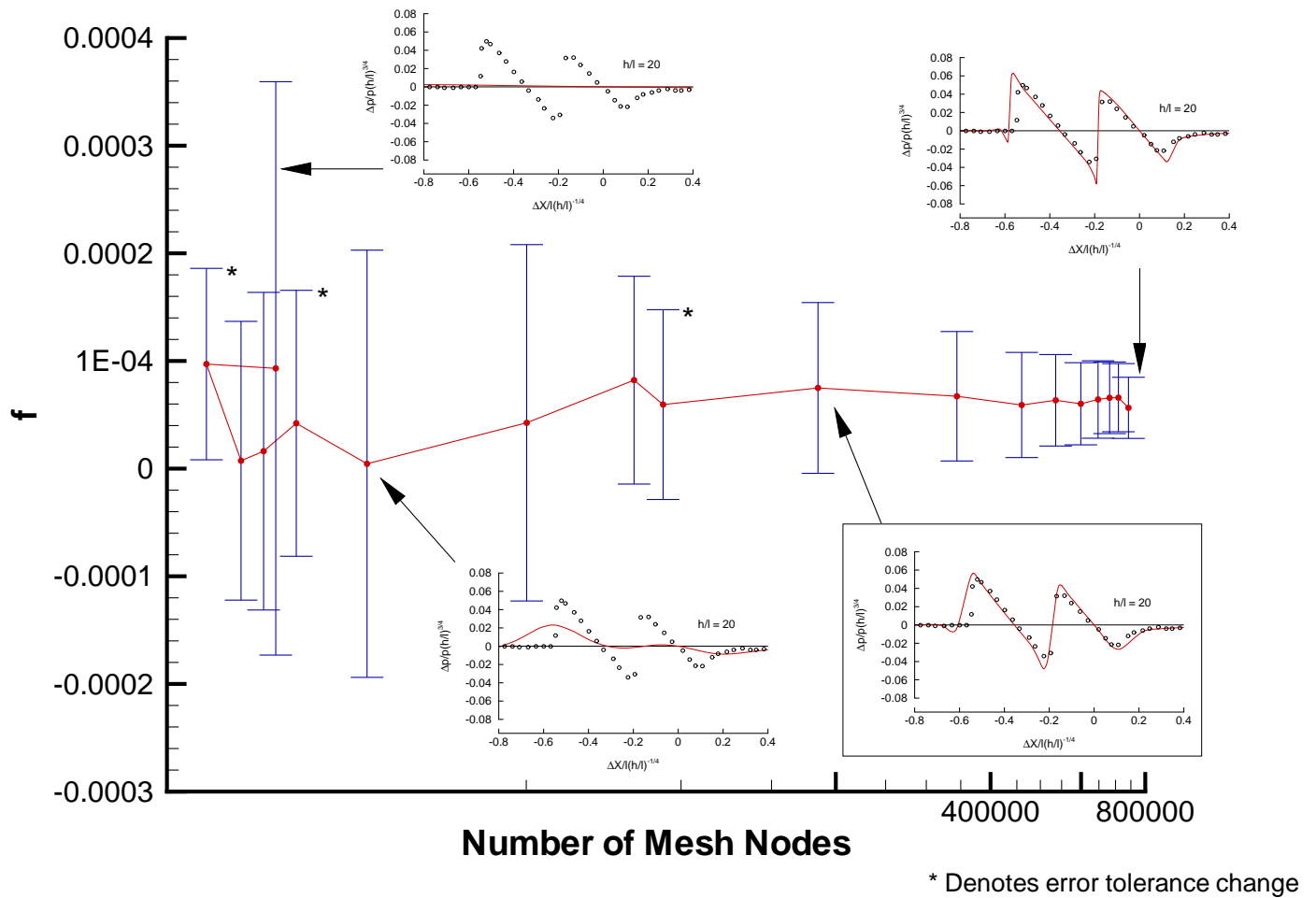


Figure 10. Double-Cone Cost Function Convergence $M = 1.41$.

used to assess solution accuracy.

The implementation of the discrete adjoint system previously described in Refs. 24, 37 and 25 has been performed using exact linearizations of the discretized residual; however, for many supersonic cases, flux limiting must be used to avoid non-physical results during the higher-order reconstruction of the solution at control volume interfaces. The linearization of these flux limiters has not been accounted for in the adjoint discretization. Unstable behavior has been observed that is similar in nature to that seen in previous work, where subtle inaccuracies in the linearization of the discretized residual were responsible for divergence of the adjoint solution procedure. The relevant contributions from the flux limiting scheme are currently being implemented so that cases which require limited reconstruction can be performed to completion.

Validation was conducted using two cone-cylinder derived test articles. The 3-D inviscid flow fields were computed for $M = 1.26$ and $M = 1.41$ without the use of flux limiters. The initial mesh and solution in all cases was far too coarse to propagate shock waves even moderately into the near-field. However, asymptotic convergence of the cost function was established automatically by the method for all cases. After multiple cycles of flow/adjoint solution, error estimation, and surface/field adaptation, very good agreement with experimental data was observed. The agreement was observed at the maximum distance for which experimental data was available, 18 and 20 body lengths. These distances were used to define the radius of the cost function integration surface. Agreement was also observed at measurement locations closer to the body. Quantifiable error bound estimates were generated along with the computed cost function at each cycle of the adaptation. No *a priori* knowledge of the test data nor the flow field physics was supplied to the automated, parallel process.

X. Acknowledgments

The authors would like to thank members of the FUN3D development team of the NASA Langley Research Center for their continuous improvement and support of the software framework upon which this work is based.

References

- ¹Whitham, G. B., "The Flow Pattern of a Supersonic Projectile," *Communications on Pure and Applied Mathematics*, Vol. 5, No. 3, Aug. 1952, pp. 301–348.
- ²Whitham, G. B., "On the Propagation of Weak Shock Waves," *Journal of Fluid Mechanics*, Vol. 1, 1956, pp. 290–318.
- ³Plotkin, K. J. and Page, J. A., "Extrapolation of Sonic Boom Signatures from CFD Solutions," AIAA Paper 2002-0922, Jan. 2002.
- ⁴Thomas, C. L., *Extrapolation of Sonic Boom Pressure Signatures by the Waveform Parameter Method*, NASA TN D-6832, June 1972.
- ⁵Plotkin, K. J., *PCBoom3 Sonic Boom Prediction Model-Version 1.0e*, Wyle Research Report WR 95-22E, Oct. 1998.
- ⁶Choi, S., Alonso, J. J., and Van der Weide, E., "Numerical and Mesh Resolution Requirements for Accurate Sonic Boom Prediction for Complete Aircraft Configurations," AIAA Paper 2004-1060, Jan. 2004.
- ⁷Warren, G. P., Anderson, W., Thomas, J. L., and Krist, S. L., "Grid Convergence for Adaptive Methods," Tech. Rep. AIAA-91-1592, June 1991.
- ⁸Monk, P. and Süli, E., "The Adaptive Computation of Far-Field Patterns by A Posteriori Error Estimation of Linear Functionals," *SIAM Journal on Numerical Analysis*, Vol. 36, 1998, pp. 251–274.
- ⁹Paraschivoiu, M., Peraire, J., and Patera, A., "A Posteriori Finite Element Bounds for Linear-functional Outputs of Elliptic Partial Differential Equations," *Computer Methods in Applied Mechanics and Engineering*, Vol. 150, 1997, pp. 289–312.
- ¹⁰Braack, M. and Rannacher, R., "Adaptive Finite Element Methods for Low-Mach Flows with Chemical Reactions," Vol. 3 of *30th Computational Fluid Dynamics*, von Karman Institute, 1999, pp. 1–93.
- ¹¹Rannacher, R., "Adaptive Galerkin Finite Element Methods for Partial Differential Equations," *Journal of Computational and Applied Mathematics*, Vol. 128, 2001, pp. 205–233.
- ¹²Becker, R. and Rannacher, R., "An optimal control approach to error control and mesh adaptation," *Acta Numerica* 2001, 2001.
- ¹³Giles, M. B. and Süli, E., "Adjoint methods for PDEs: a posteriori error analysis and postprocessing by duality," *Acta Numerica*, Vol. 11, 2002, pp. 145–236.
- ¹⁴Peraire, J. and Patera, A. T., "Asymptotic a posteriori finite element bounds for the outputs of noncoercive problems: the Helmholtz and Burgers equations," *Computer Methods in Applied Mechanics and Engineering*, Vol. 171, 1999, pp. 77–86.
- ¹⁵Barth, T. and Deconinck, H., editors, *Error Estimation and Adaptive Discretization Methods in Computational Fluid Dynamics*, Number 25 in Lecture Notes in Computational Science and Engineering, Springer-Verlag, 2002.
- ¹⁶Pierce, N. A. and Giles, M. B., "Adjoint Recovery of Superconvergent Functionals from PDE Approximations," *SIAM Review*, Vol. 42, No. 2, 2000, pp. 247–264.
- ¹⁷Müller, J. D. and Giles, M. B., "Solution Adaptive Mesh Refinement Using Adjoint Error Analysis," AIAA Paper 2001-2550, 2001.
- ¹⁸Venditti, D. A. and Darmofal, D. L., "Anisotropic Grid Adaptation for Functional Outputs: Application to Two-Dimensional Viscous Flows," *Journal of Computational Physics*, Vol. 187, 2003, pp. 22–46.
- ¹⁹Venditti, D. A., *Grid Adaptation for Functional Outputs of Compressible Flow Simulations*, Ph.D. thesis, Massachusetts Institute of Technology, Cambridge, MA, 2002.

- ²⁰Park, M. A., "Adjoint-Based, Three-Dimensional Error Prediction and Grid Adaptation," *AIAA Journal*, Vol. 42, No. 9, September 2004, pp. 1854–1862, See also AIAA Paper 2002–3286.
- ²¹Park, M. A., "Three-Dimensional Turbulent RANS Adjoint-Based Error Correction," AIAA Paper 2003-3849, June 2003.
- ²²Lee-Rausch, E. M., Park, M. A., Jones, W. T., Hammond, D. P., and Nielsen, E. J., "Application of Parallel Adjoint-Based Error Estimate and Anisotropic Grid Adaptation for Three-Dimensional Aerospace Configurations," AIAA Paper 2005-4842, June 2005.
- ²³Anderson, W. K. and Bonhaus, D. L., "An Implicit Upwind Algorithm for Computing Turbulent Flows on Unstructured Grids," *Computers and Fluids*, Vol. 23, No. 1, 1994, pp. 1–22.
- ²⁴Anderson, W. K., Rausch, R. D., and Bonhaus, D. L., "Implicit/Multigrid Algorithm for Incompressible Turbulent Flows on Unstructured Grids," *Journal of Computational Fluids*, Vol. 128, 1996, pp. 391–408.
- ²⁵Nielsen, E. J., *Aerodynamic Design Sensitivities on an Unstructured Mesh Using the Navier-Stokes Equations and a Discrete Adjoint Formulation*, Ph.D. thesis, Virginia Polytechnic Institute and State University, Blacksburg, VA, 1998.
- ²⁶Nielsen, E. J., Lu, J., Park, M. A., and Darmofal, D. L., "An Implicit, Exact Dual Adjoint Solution Method Implicit, Exact Dual Adjoint Solution Method for Turbulent Flows on Unstructured Grids," *Computers and Fluids*, Vol. 33, No. 9, 2004, pp. 1131–1155, See also AIAA Paper 2003–0272.
- ²⁷Spalart, P. R. and Allmaras, S. R., "One-Equation Turbulence Model for Aerodynamic Flows," AIAA Paper 92–0429, 1992.
- ²⁸Taylor, A. C., Green, L. L., Newman, P. A., and Putko, M. M., "Some Advanced Concepts in Discrete Aerodynamic Sensitivity Analysis," AIAA Paper 2001–2529, 2001.
- ²⁹Giles, M., Duta, M., Müller, J.-D., and Pierce, N., "Algorithm Developments for Discrete Adjoint Methods," *AIAA Journal*, Vol. 41, No. 2, 2003, pp. 198–205, See also AIAA Paper 2001–2596.
- ³⁰Park, M. A., "Parallel, Distributed Memory Execution of Nearest-Neighbor Grid Adaptation Operations: refine," Class Project 21W.783, Massachusetts Institute of Technology, Cambridge, MA, 2005.
- ³¹Jones, W. T., "An Open Framework for Unstructured Grid Generation," AIAA Paper 2002-3192, June 2002.
- ³²Jones, W. T., "GridEx – An Integrated Grid Generation Package for CFD," AIAA Paper 2003–4129, 2003.
- ³³Haimes, R., "CAPRI: Computational Analysis PRogramming Interface," Massachusetts Institute of Technology, Cambridge, MA, 2002.
- ³⁴Haimes, R., "Automatic Generation of CFD-Ready Surface Triangulations from CAD Geometry," AIAA Paper 99–0776, 1999.
- ³⁵Haimes, R., "CAPRI: Computational Analysis PRogramming Interface," *Proceedings of the 6th International Conference on Numerical Grid Generation in Computational Field Simulations*, July 1998.
- ³⁶Carlson, H., Mack, R., and Morris, O., *A Wind-Tunnel Investigation of the Effect of Body Shape on Sonic-Boom Pressure Distributions*, NASA TN D-3106, 1965.
- ³⁷Nielsen, E. J. and Anderson, W. K., "Recent Improvements in Aerodynamic Design Optimization on Unstructured Meshes," AIAA Paper 2001–0596, 2001.